Bed shear stress estimation on an open intertidal flat using in situ measurements

Zhu, Qin; van Prooijen, Bram; Wang, Zhengbing ; Ma, Y.X.; Yang, SL

DOI
10.1016/j.ecss.2016.08.028

Publication date
2016

Document Version
Proof

Published in
Estuarine, Coastal and Shelf Science

Citation (APA)
Zhu, Q., van Prooijen, B., Wang, Z., Ma, Y. X., & Yang, SL. (2016). Bed shear stress estimation on an open intertidal flat using in situ measurements. *Estuarine, Coastal and Shelf Science*, *182*(Part A), 190-201. https://doi.org/10.1016/j.ecss.2016.08.028

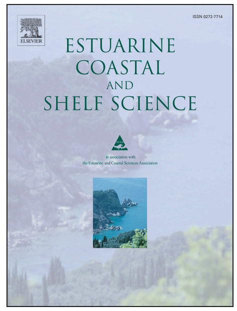

Bed shear stress estimation on an open intertidal flat using in situ measurements

Q. Zhu, B.C. van Prooijen, Z.B. Wang, Y.X. Ma, S.L. Yang

PII: S0272-7714(16)30283-9

DOI: 10.1016/j.ecss.2016.08.028

Reference: YECSS 5218

To appear in: *Estuarine, Coastal and Shelf Science*

Received Date: 27 February 2016

Revised Date: 24 August 2016

Accepted Date: 26 August 2016

Please cite this article as: Zhu, Q., van Prooijen, B.C., Wang, Z.B., Ma, Y.X., Yang, S.L., Bed shear stress estimation on an open intertidal flat using in situ measurements, *Estuarine, Coastal and Shelf Science* (2016), doi: 10.1016/j.ecss.2016.08.028.

Bed shear stress estimation on an open intertidal flat using in situ measurements

Q. Zhu[1,2], B.C. van Prooijen[2], Z.B. Wang[1,2,3], Y.X. Ma[4], S.L. Yang[1,*]

1. State Key Laboratory of Estuarine and Coastal Research, East China Normal University, Shanghai 200062, China

2. Department of Hydraulic Engineering, Faculty Civil Engineering and Geosciences, Delft University of Technology, P.O. Box 5048, 2600 GA Delft, The Netherlands

3. Deltares, P.O. Box 177, 2600 MH Delft, The Netherlands

4. Department of Oceanography and Coastal Sciences, Louisiana State University, Baton Rouge, LA 70803, USA

*Corresponding author: slyang@sklec.ecnu.edu.cn

Abstract

Accurate estimations for the bed shear stress are essential to predict the erosion and deposition processes in estuaries and coasts. This study used high-frequency in situ measurements of water depths and near-bed velocities to estimate bed shear stress on an open intertidal flat in the Yangtze Delta, China. To determine the current-induced bed shear stress (τ_c) the in situ near-bed velocities were first decomposed from the turbulent velocity into separate wave orbital velocities using two approaches: a moving average (MA) and energy spectrum analysis (ESA). τ_c was then calculated and evaluated using the log-profile (LP), turbulent kinetic energy (TKE), modified TKE (TKEw), Reynolds stress (RS), and inertial dissipation (ID) methods. Wave-induced bed shear stress (τ_w) was estimated using classic linear wave theory. The total bed shear stress (τ_{cw}) was determined based on the Grant–Madsen wave–current interaction model (WCI). The results demonstrate that when the ratio of significant wave height to water depth (H_s/h) is greater than 0.25, τ_{cw} is significantly overestimated because the vertical velocity fluctuations are contaminated by the surface waves generated by high winds. In addition, wind enhances the total bed shear stress as a result of the increases in both τ_w and τ_c generated by the greater wave height and reinforcing of vertical turbulence, respectively. From a comparison of these various methods, the TKEw method associated with ESA decomposition was found to be the best approach because: (1) this method generates the highest mean index of agreement; (2) it uses vertical velocities that are less affected by Doppler noise; and (3) it is less sensitive to the near-bed stratification structure and uncertainty in bed location and roughness.

Keywords: bed shear stress; wave-turbulence decomposition; wind; combined wave–current action; intertidal flat; Yangtze River Delta

1. Introduction

Intertidal flats are ubiquitous in estuarine and coastal areas worldwide. These landforms have been, and still are, used as a source of land that can be reclaimed from the sea. However, it is becoming increasingly apparent that healthy tidal flats provide many other important benefits for both the local population and the natural environment. For example, they protect coastal areas by forming a buffer between land and sea that can attenuate wave energy. Furthermore, these areas provide essential environmental functions, such as habitats and nursery grounds for a wide range of wildlife, and as natural sewage purification systems. However, the impact of natural and human interference, such as sea level rise and the damming of rivers, can result in a reduction in the area covered by tidal flats, and the Yangtze tidal flats in China are one such example (Yang et al., 2011). The precise processes responsible for the degeneration of tidal flats are still not fully understood, and various aspects factors that affect such environments make it difficult to predict the future of tidal flats. One of these key factors is the definition of bed shear stress.

Bed shear stress is a critical parameter in sediment dynamics on tidal flats, especially in the calculation of erosion rates (Friedrichs et al., 2000; Friedrichs and Wright, 2004; Wang et al., 2013), and the total bed shear stress is the combined contributions from waves and currents. Numerous studies have estimated the total bed shear stress by means of a wave–current interaction model (Grant and Madsen, 1979; Fredsøe, 1984; Christoffersen and Jonsson, 1985; O'Connor and Yoo, 1988; Huyng-Thanh and Temperville, 1990; Myrhaug and Slaattelid, 1990; van Rijn, 1993; Davies and Gerritsen, 1994; Shi et al., 2015), and an overview is given by Soulsby (2005). These wave–current interaction models have been widely applied in numerical models of estuarine and coastal areas (Villaret and Latteux, 1992; Lesser et al., 2004; Warner et al., 2008; Shi et al., 2016). The waves and currents interact in a non-linear way, leading to a total bed shear stress that is not a simple linear addition of wave-induced and current-induced bed shear stress.

The wave–current interaction model (WCI) is an algebraic equation that combines the pure wave-induced and pure current-induced bed shear stresses to obtain the total bed shear stress that accounts for the direction of the waves and currents. The determination of the wave-induced bed shear stress and the current-induced bed shear stress is based on bulk parameters. The wave-induced bed shear stress is generally obtained by using a linear wave theory (Green and Coco, 2007) for a given wave height, wave period, and water depth. The bed shear stresses associated with currents are generally estimated based on the assumption of stationary uniform flow and using the log law; however, this assumption is often violated.

The direct measurement of bed shear stresses presents some difficulties (Grant and Madsen, 1979; Soulsby, 2005). Further advances in acoustic instruments have allowed systematic velocity measurements to be made over longer periods, at higher sampling rates and with greater accuracy (Wang et al., 2006; 2012). The ADV (Acoustic Doppler Velocimeter) makes high-frequency measurements of the 3D velocities at a single point, whereas the ADCP (Acoustic Doppler Current Profiler) measures velocities over a profile. Despite these improvements, the difficulty remains of selecting the most appropriate theory to obtain the current-induced bed shear stress. The most widely used theories are: (1) the LP (log-profile) method; (2) the TKE (turbulent kinetic energy) method; (3) the TKEw (modified TKE) method; (4) the Reynolds stress (RS) method; and (5) the ID (inertial dissipation) method. The LP method uses the mean component of a velocity profile series, whereas the other methods use the turbulent velocity. Kim et al. (2000) systematically compared the current-induced bed shear stresses obtained using the LP, TKE, RS, and ID methods, and found differences of up to 19% between the TKE and LP methods. No significant wave events were recorded. They suggested that all methods should be applied simultaneously to help better estimate bed shear stress. On many tidal flats, the conditions are generally more complex than in their study. As the water depth changes significantly, the relative locations of the fixed measurement positions change. Due to the shallow water depth, wind-driven flow may have a significant influence and disturb the logarithmic flow profile.

Having recognised this inaccuracy, several studies have been conducted to compare some of the above methods of obtaining the bed shear stress (Kim et al., 2000; Andersen et al., 2007). One of the assumptions is that the vertical component of velocity is not contaminated by waves (see also Stapleton and Huntley, 1995). Wave motion is expected to have a great impact on the velocity distribution near the bed on tidal flats, especially in wavy conditions; e.g., during storms or typhoons.

In this paper, we compare the methods used to determine the bed shear stress on intertidal flats. In such areas, the assumptions on which the methods used to determine current-induced bed shear stress are based, are possibly violated. We conducted high-frequency, in situ measurements of water depth and near-bed velocities, as well as near-bed current profiles, on an intertidal flat in the Yangtze Estuary, China. Our specific goals were to: (1) investigate how, and by how much, the wind influences the near-bed velocity distribution; (2) compare and summarize the calculation methods used to determine the total bed shear stress; and (3) develop an optimum solution for estimating the total bed shear stress in intertidal areas.

2. Study area and instrumentation

In situ observations were conducted on an exposed tidal flat on the Eastern Chongming mudflat, located on the Yangtze River Delta (Figure 1A). The tides in the Yangtze Estuary are mixed semidiurnal, and the average tidal range, based on records from the Sheshan gauging station, which is 20 km east of the study site, is 2.5 m, reaching 3.5–4.0 m during spring tides. The monsoon-driven winds are southeasterly in summer and northwesterly in winter. The wind speed in this area is highly variable, with multi-year averages of 3.5–4.5 m/s, and a maximum value of 36 m/s recorded at the Sheshan gauging stations (GSCI, 1988; Yang et al., 2008).

Figure 1

The southern part of the Eastern Chongming tidal flat is interrupted by a secondary channel that runs in an east–northeast direction. The observation site, which is close to mean sea level, is 1.65 km seaward of the sea wall. The bed sediment on the present mudflat is mainly silt (median grain size < 63 μm), with a coarse silt (32–64 μm) fraction that exceeds 50% (Yang et al., 2008).

Our observations were carried out from July 23 to August 3, 2011. Wave heights, wave periods, and water depths were measured using a self-logging sensor, the SBE-26plus Seagauge (Sea-Bird Electronics, Washington, USA), which was developed for wave monitoring using a data collection system comprising a 45-psia Paroscientific Digiquartze connected to an oil-filled tube via the pressure port (Sea-Bird Electronics, 2007). The instrument was horizontally placed on the sediment surface with the pressure probe located 8 cm above the sediment surface (Figure 1C). The measuring burst interval was 10 minutes. Pressure data were collected at a frequency of 4 Hz over a duration of 256 seconds, yielding 1024 measurements per burst.

An ADCP (1.0 MHz high-resolution profiler, Nortek AS, Norway) was used to measure 3D current velocity profiles. The burst interval was 5 minutes. Each velocity profile is the mean value collected at a frequency of 1 Hz over a duration of 60 seconds. The ADCP was attached to the tripod with the transmitters facing downwards and located 85 cm above the sediment surface. The blanking distance was 40 cm, and the cell size was set to 2 cm.

An ADV (6.0 MHz vector current meter, Nortek AS, Norway) was used to measure the 3D velocity at a high sampling frequency in a small measurement volume (2.65 cm^3). The sampling volume was located 9.3 cm above the bed. The ADV recorded velocities and pressure with a burst interval of 5 minutes, and for a period of 90 seconds at a frequency of 8 Hz. The water pressure in a high sampling rate, measured by a silicone piezoresistive pressure sensor (Nortek AS, 2005), was also used to analyse wave characteristics. Finally, wind data at 122.25°E, 31.5°N were obtained from the European Centre for Medium-Range Forecasts (ECMWF) at an interval of three hours.

3. Bed shear stress formulations

3.1 Bed shear stress caused by combined wave–current action

To determine the bed shear stress caused by combined wave–current action (referred to as total bed shear stress hereafter) (τ_{cw}, Pa), we used the method of Grant and Madsen (1979), which introduces a combined wave–current friction factor and is expressed as

$$\tau_{cw} = \sqrt{\left(\tau_w + \tau_c\left|\cos\varphi_{cw}\right|\right)^2 + \left(\tau_c\left|\sin\varphi_{cw}\right|\right)^2} \tag{1}$$

where τ_w (Pa) and τ_c (Pa) are the wave- and current-induced bed shear stress, respectively, and ϕ_{cw} (°) is the angle between the current direction ϕ_c (°) and the wave propagation direction ϕ_w (°). In this equation, four parameters are required to calculate the total bed shear stress: τ_w, τ_c, ϕ_c, and ϕ_w.

3.2 Wave-induced bed shear stress

Wave-induced bed shear stress (τ_w) is usually obtained from the significant/peak bottom orbital velocity U_δ (m/s) and wave friction coefficient f_w (van Rijn, 1993):

$$\tau_w = \frac{1}{4}\rho_w f_w U_\delta^2 \tag{2}$$

where ρ_w is the water density (kg/m^3). At the edge of the wave boundary layer, the peak orbital excursion (A_δ) and peak orbital velocity (U_δ) can be respectively expressed as

$$A_\delta = \frac{H}{2\sinh(kh)} \tag{3}$$

$$U_\delta = \omega A_\delta = \frac{\pi H}{T\ \sinh(kh)} \tag{4}$$

where H is the wave height (m), k (= $2\pi/L$ where $L = (gT^2/2\pi)\tanh(kh)$ and is the wave length) is the wave number (m^{-1}), h is water depth (m), ω is angular velocity (s^{-1}), and T

is the wave period (s). The wave friction coefficient f_w depends on the hydraulic regime (Soulsby, 1997):

$$f_w = \begin{cases} 2\,\mathrm{Re}_w^{-0.5} & , \ \mathrm{Re}_w \le 10^5 \ \text{(laminar)} \\ 0.0521\mathrm{Re}_w^{-0.187} & , \ \mathrm{Re}_w > 10^5 \ \text{(smooth turbulent)} \\ 0.237\, r^{-0.52} & , \ \text{(rough turbulent)} \end{cases} \quad (5)$$

where $\mathrm{Re}_w = \dfrac{U_\delta A_\delta}{\nu}$ and $r = \dfrac{A_\delta}{k_s}$ are the wave Reynolds number and relative roughness, respectively. k_s is the Nikuradse roughness given by $k_s = 2.5 d_{50}$ where d_{50} is the median grain size of the bed sediment, and ν is the kinematic viscosity of water (m^2/s).

In practice, the significant wave height H_s and significant wave period T_s are used in the equations mentioned above. The wave parameters were obtained using the 'SEASOFT for Waves' software package for the SBE-26plus, and by analysing high-frequency water level elevation data obtained by ADV via zero-crossing and spectral estimates (Table A.1).

3.3 Current-induced bed shear stress

The instantaneous velocity in a 3D orthogonal coordinate system can be expressed as $\boldsymbol{U} = u\hat{i} + v\hat{j} + w\hat{k}$, where u, v, and w are the instantaneous magnitudes in the three orthogonal directions $\hat{i}$, $\hat{j}$, and $\hat{k}$, respectively. The flow across tidal flats is subject to bed friction, resulting in a turbulent boundary layer that can extend to the water surface in the typically shallow conditions (Whitehouse et al., 2000). In this layer, current velocity is composed of a mean component ($*_m$) and a fluctuating component. The fluctuating component can be further decomposed into two parts: the wave orbital motion ($*_w$) and turbulence ($*_t$), resulting in the following:

$$\begin{aligned} u &= u_m + u_w + u_t \\ v &= u_m + v_w + v_t \\ w &= u_m + v_w + w_t \end{aligned} \quad (6)$$

For the present study, each measurement period lasted for 90 s. Over such a short sampling duration, we assumed that the velocity series follows a linear increasing/decreasing trend. Five methods were applied to estimate the current-induced bed shear stress in this paper: the LP method uses mean velocities, whereas the TKE, TKEw, RS, and ID methods use fluctuating velocities.

The LP method is based on the assumption that the burst-mean horizontal current speed ($U_c = \sqrt{u_m^2 + v_m^2}$) profile in the boundary layer follows a logarithmic distribution:

$$U_c(z) = \frac{U_{*c}}{\kappa} \ln\left(\frac{z}{z_0}\right) \tag{7}$$

where $U_c(z)$ (m/s) is the current speed at the height above the bed, z (m); U_{*c} (m/s) is the friction velocity; κ is Von Kármán's dimensionless constant (= 0.4); and z_0 (m) is the roughness length, which is the distance from the bed at which the flow reaches zero if the flow profile strictly follows the logarithmic law. By regressing the current speed U_c(z) against ln(z) using the least-squares method, U_{*c} and z_0 can be calculated from the gradient A and intercept B as follows:

$$\begin{aligned} U_{*c} &= \kappa A \\ z_0 &= e^{-\frac{B}{A}} \end{aligned} \tag{8}$$

We used internal consistency analysis (Collins et al., 1998) to examine whether the results derived from the $U_c(z)$–ln(z) relationship can be used to characterize boundary layer conditions. A linear relationship must exist between the shear velocity U_{*c} derived from Equation (7), and the current speed within the boundary layer ($U_{z'}$, here taken as U_{40}, which is the current speed at 40 cm above the bed), written as:

$$U_{*c} = aU_{z'} + b \tag{9}$$

To pass the internal consistency analysis, four requirements must be met: 1) the linear correlation between U_{*c} and $U_{z'}$ must exceed the appropriate significance level; 2) the regressed intercept should be small ($b \approx 0$); 3) z_0 obtained from the slope of the regression line should be similar to that derived using the $U_c(z)$–ln(z) regression:

$$a = \frac{\kappa}{\ln\left(\frac{z}{z_0}\right)} \tag{10}$$

and 4) the value of $C_D(z')$, which is the drag coefficient at a height of z' (40 cm in the present study), derived on the basis of slope a, should be consistent with

$$C_D(z') = \frac{U_{*c}^2}{U_{z'}^2} \tag{11}$$

The current-induced bed shear stress (τ_c, Pa) is subsequently calculated according as follows:

$$\tau_{c,LP} = \rho_w C_D(z')U_{z'}^2 \tag{12}$$

The second momentum methods are listed in Table A.2. The TKE method and the TKEw method are based on the assumption that the bed shear stress scales linearly with the intensity of velocity fluctuations. To minimize the noise from the orbital motion of waves in the horizontal components, only the vertical fluctuations are used in the TKEw method. Minimizing the effects of waves has also been achieved using band-pass filtering (see below). In the RS method, it is assumed that the measured covariance between horizontal and vertical fluctuations is close to the value near the bed. Soulsby and Humphery (1990) argued that it is not necessary to separate out the wave orbital velocities, as the vertical wave-induced velocity is both small and in quadrature with the horizontal component.

In the ID method, the friction velocity is derived by assuming a first-order balance between shear production and energy dissipation with deployment of the 1D spectrum applicable to the inertial dissipation range (Huntley, 1988; Kim et al., 2000), giving

$$U_* = (\kappa z)^{1/3}\left(\frac{S_i(k)k^{5/3}}{\alpha_\mathrm{i}}\right)^{1/2} \tag{13}$$

where $\alpha_i (i = 1, 2, 3)$ are 1D Kolmogorov constants, with *i*=1 and *i*=2 denoting directions parallel and transverse to the main flow, respectively, and *i*=3 denoting the vertical direction. In locally isotropic turbulence, $\alpha_1 = 0.51$, and $\alpha_2 = \alpha_3 = 4/3\alpha_1 = 0.68$ (Green, 1992). The frozen turbulence hypothesis, which assumes $S(k)k = S(f)f$ with $k = 2\pi f / U_c$, is then applied to transfer Equation (13) from the wave number (*k*) domain to the frequency (*f*) domain (Huntley, 1988). In the inertial subrange, $S_w(f)f^{5/3}$ is constant. In practice, the average value around the maximum value is used to represent $S_w(f)f^{5/3}$.

3.4 Current and wave directions

The current direction φ_c is derived from the mean value of the two horizontal velocity components u_m and v_m:

$$\varphi_c = \arctan\left(\frac{v_m}{u_m}\right) \tag{14}$$

The wave direction φ_w is defined similarly, but based on the wave-induced orbital velocities u_w and v_w. Given a series of φ_w in a measurement burst, the wave direction is defined as the direction with the maximum number of counts. Two peaks in the direction counts, which are theoretically in a difference of 180°, can be found (Figure 2). As $|\cos\varphi_{cw}|$ and $|\sin\varphi_{cw}|$ are used in the WCI model, only one of the two peak directions is required. Accordingly, the counts between 180° and 360° are superimposed on those between 0° and 180°. A count every 5° was used in the present study.

Figure 2

3.5 Wave–turbulence decomposition

The second momentum methods (TKE, TKEw, and ID) use the turbulent velocities only, so turbulent velocities are separated from the mixed wave–turbulent velocities. Two approaches were used to decompose the wave velocities from the turbulent velocities: a moving average (MA) (Williams et al., 2003) and energy spectrum analysis (ESA) (Soulsby and Humphery, 1990). The band-pass filter method of Meirelles et al. (2015) is similar to the ESA method and gives similar results.

Williams et al. (2003) applied a simple MA filter that uses the mean of the previous *N* values to forecast the value at time *t*, as follows:

$$F_t = \frac{1}{N}\sum_{i=1}^{N} A_{t-i+1} \tag{15}$$

where F_t is the forecast value at time *t*, *N* is the number of previous data points to be included in the MA, and A_t is the actual value at time *t*. Williams et al. (2003) used a 1-second MA to resample the original signal and extract the bulk wave-induced velocities.

The ESA technique was developed by Soulsby and Humphery (1990) to split the variance without separating the instantaneous time series (Figure 3). The burst velocity series is first detrended to get combined wave–turbulent velocities u_w+u_t. The area under the energy spectrum $S_u(f)$ equals the total variance $\overline{(u_w + u_t)^2}$. A log–log plot (Figure 3C) reveals that the spectrum is a wave velocity spectrum, with a peak near 0.3 Hz and a characteristic f^{-5} power law decaying at higher wave frequencies, superimposed on a conventional turbulence spectrum, with a characteristic $f^{-5/3}$ slope in the inertial subrange. This spectrum is further separated by a straight red dotted line in Figure 3C, and the area above this line contributes to the wave variance $\overline{u_w^2}$, whereas the area below the line contributes to the turbulence variance $\overline{u_t^2}$.

Figure 3

In the separated turbulent velocity spectrum, power densities of low frequency indicate the turbulent kinetic energy contributed by turbulence in energy containing range, while power densities in high frequency domain is in inertial range.

3.6 Index of agreement

Intercomparisons among the bed shear stresses estimated using these approaches was carried out using the index of agreement *I*. This index is introduced to quantitatively determine the similarity between two methods of estimating the same variable (Willmott, 1981):

$$I = 1 - \frac{\sum (x-y)^2}{\sum (|x-\bar{y}| + |y-\bar{y}|)^2} \tag{16}$$

where *x* and *y* are the two datasets being compared; $0 < I \leq 1$. The larger the value *I* is, the higher level of similarity the two datasets *x* and *y* is. *I* = 1 indicates perfect agreement.

4. Results

4.1 Spectra and Decomposition

Water level and velocity spectra were determined for each burst interval, and these spectral results are combined with contour plots in Figure 4B–E. As the measurement location falls dry at low water, no data were collected during these periods. Over the neap tides in the first part of the sampling period, some tides did not inundate the monitoring site. Three periods can be identified based on the wind conditions (Figure 4A): Period I (July 23–July 31); Period II (July 31–August 02), and Period III (August 02–August 03).

Figure 4B shows the contours of the energy density spectra of the water level fluctuations above the datum of the original bed level. In Period I, before July 31, a single peak is evident at a frequency around 0.32 Hz. No clear peaks are seen over Period II, indicating that wave heights were low. During Period III, two peaks occur around a frequency at 0.32 and at 0.1 Hz, and this indicates that the wave regime was dominated by locally generated waves over Period I, whereas offshore winds and swell dominated wave activity during Period III.

Figure 4

Figure 4C–E shows the energy spectra derived from the velocity fluctuations in the three orthogonal directions. Similar to the water level spectra, a double-peaked spectrum is seen in Period III for the northward velocities (*v*), and this is more clearly highlighted in the averaged spectra (Figure 5C). The velocity spectra for the northward direction have a similar shape to the spectra of the water level fluctuations, which implies that the near-bed velocities in the wave propagation direction are significantly affected by wave motion. Based on the 'wind wave' and 'wind wave + swell' conditions, two corresponding pass-bands were applied to the ESA wave–turbulence decomposition methods (Figure 5).

Figure 5

For the spectrum of the vertical velocity component, a peak occurs in the velocity spectrum at the same frequency as for the water level spectrum during Period I (Figure 5A). No clear peak is seen in the vertical velocity spectrum for the calmer Period II (Figure 5B). Furthermore, on average the waves contribute 64% to the spectral density of the vertical wave-turbulence energy spectrum, with a maximum contribution of 95%.

Our results suggest that the near-bed velocity fluctuations were caused in part by waves. Even the vertical fluctuations, which are often assumed to be free of wave influence, are highly contaminated by the waves. Consequently, a decomposition of the velocity fluctuations is needed to separate waves and turbulent motion. Figure 4B shows the velocity spectrum smoothed using an MA with a window of one second and the spectrum obtained after BP filtering with the pass-bands indicated in Figure 5.

A peak in the wave frequency band remains in the energy spectra of turbulent velocities obtained using the MA method. This indicates an incomplete separation of wave–turbulence decomposition. Moreover, in the low-frequency domain, the MA provides a low estimation of the turbulence spectral density.

4.2 Bed shear stresses

4.2.1 Wave-induced bed shear stress

The wave-induced bed shear stresses obtained using the different approaches were in good agreement with each other. The index of agreement (*I*) of each comparison was above 0.94 (Table 1). The 'SEASOFT for Waves' software package for the SBE-26plus obtained wave characteristics H_s and T_s using zero-crossing method (Sea-Bird Electronics, 2007). Theoretically, wave parameters obtained using pressure dataset from ADV and SBE-26plus using the zero-crossing method should be in accordance with each other. The instrument-dependent differences were probably caused by differences in the probe type and deployment settings (sampling frequency and duration). For the same ADV pressure dataset, zero-crossing and spectral estimation provide close τ_w values, with *I* reaching 0.98. Zero-crossing counts the water level going to equilibrium positions, while spectral estimation uses Fourier transform. They are expected to gain the similar values of wave parameters by signal processing approach. As the three approaches provide similar estimates of τ_w, the results obtained from the spectral estimations based on the ADV pressure data are used in the following analysis.

Table 1

During windy conditions, the orbital velocity distribution indicates that waves propagate in a north-westnorth direction, which is the same direction as the prevailing wind. During the calm conditions around August 1st, the wave direction over one tidal cycle became divergent when the wind direction moved offshore (Figure 2G).

4.2.2 Current-induced bed shear stress

The average value of the current-induced bed shear stress, τ_c, was 2.3 times larger than the wave-induced bed shear stress τ_w, indicating that currents and waves acted in competition in the present study area, whereas current-induced forces have a greater effect on the bed than do waves (Figure 2I).

Figure 6

Figure 6 demonstrates that the time series of τ_c obtained using different methods show similar variation patterns during a tidal cycle. However, agreement in the magnitude of τ_c is weaker under windy conditions than under calm weather. According to our intercomparison analysis, indices of agreement vary around 0.86 (from 0.5 to 1) during calm conditions, but around 0.58 (from 0.25 to 0.86) during windy conditions (Table 2).

Table 2

4.2.3 Total bed shear stress

The total bed shear stress under combined wave–current action obtained using the methods outlined above, varied from 0 to 3 Pa with an average of 0.65 Pa. The largest estimated value of averaged τ_{cw} was two times higher than the lowest estimate (Table 2). As with τ_c, values of τ_{cw} calculated using the different methods show more consistency under calm conditions (Figure 6B and 6D). Regarding the wave–turbulence decomposition methods, the MA method provides the higher estimates, and the ESA method provides the lower estimates.

The TKEw method, which uses ESA decomposition (TKEw-ESA), provided a moderate mean τ_{cw} value and generated the highest mean index of agreement, which is the average of the agreement level (*I*) values of this method with all the other methods. The mean value of τ_{cw} obtained from the TKEw-ESA method was 2.5 times greater under windy conditions than under calm conditions. Over a calm tidal cycle, τ_{cw} values decreased to the minimum value around high tide when current speeds are at their lowest (Figure 6D); however, τ_{cw} remained high over the course of a windy tidal cycle, even during slack water (Figure 6C).

5. Discussion

Several studies have compared the various approaches to estimating bed shear stress and have pointed out that each method has its advantages and disadvantages (Kim et al., 2000; Verney et al., 2006; Andersen et al., 2007; Salehi and Strom, 2012). They also concluded that in current-dominated environments, the different methods all tend to provide similar estimates, although the often-used LP method is better than other methods because it requires less data-set filtration (Andersen et al., 2007) and produces less scatter (Salehi and Strom, 2012). However, in the presence of waves it is difficult to identify the best method without knowing the true value of the bed shear stress. By focusing on the trends in time series, the magnitude of the estimation, degree of scatter, and the correlation with the SNR (signal-noise ratio), the TKE, TKEw, and RS methods have been identified as the most appropriate estimators of bed shear stress (Kim et al., 2000; Salehi and Strom, 2012). In the following discussion, we focus mainly on the limitations of each method in an attempt to identify the most appropriate method of estimating bed shear stress in combined wave–current environments.

We used internal consistency analysis to examine whether the results derived from the $U_c(z)$ –ln(z) relationship can be used to characterize boundary layer conditions. Estimations of τ_c by different approaches bring uncertainty in the definition of τ_{cw}. The LP method is a first moment method. This method requires a logarithmic velocity distribution, which may not be the case in reality. The present study shows a pass rate of 90% after internal consistency analysis, and most of the unpassed profiles were recorded at slack water, when the tidal current starts to rotate; this is in agreement with previous studies (Collins et al., 1998; Wang et al., 2013; Zhu et al., 2014; Liu and Wu, 2015). Another limitation of the LP method is that it requires a fixed bed level that cannot vary with time. In reality, however, the bed level varies in the intertidal area. In energetic regions, where bed level change might be on the order of centimetres over a single tidal cycle, the error is caused by a vertical shift in the current velocity profile. For longer-duration measurements that incorporate extreme events, the error could be even larger when bed level variations may be on the order of decimetres.

Other mechanisms that violated the assumption of a logarithmic velocity distribution in shallow water include: unsteady flow (e.g., acceleration/deceleration of flow), stratification in the water column and transport of material as bed load, wind influencing the velocity profile by adding wave effects and producing variable velocity close to the water surface, and topography-induced secondary flows (Wilkinson, 1985; Gross et al., 1992; Friedrichs and Wright, 1997; Collins et al., 1998). For these reasons, the pass rate of internal consistency analysis may be lower, even reaching 0% at some locations (Collins et al., 1998). Note that a logarithmic velocity profile only guarantees the estimation of tidal-induced bed shear stress. The LP method would not detect the bed shear stress caused by wind-induced turbulent currents.

All estimates made using second momentum (TKE, TKEw, ID, and RS) are sensitive to probe height. These techniques require the ADV sampling volume to be within the log layer, but high enough to avoid damping effects and near-bed stratification. Andersen et al. (2007) pointed out that placing the sampling volume at 1–4 cm above the bed might be too close to the bed and that fluctuations in vertical velocities would be dampened. This might be the reason why LP method was preferred rather than the second momentum methods. Among the second momentum methods, the ID method assumes that shear production and energy dissipation are equivalent. This means that an incomplete separation may lead to errors in the estimation of τ_c. Following the correction expression proposed by Huntley (1988), Kim et al. (2000) proposed a critical height of 35 cm, below which the full production–dissipation separation may not be ensured. In the present study, the ADV sampling volume height of 9.3 cm seems to be too low for ID estimation.

One of the key assumptions in the second momentum methods is that the fluctuating velocities measured in the vertical dimension are not contaminated by wave orbital motion, and this assumption has been used in many other studies (Kim et al., 2000; Andersen et al., 2007; Wang, 2007). This assumption has the largest impact on the TKEw method, which only uses the vertical turbulent velocities. Without wave-turbulence decomposition, τ_{cw} could be overestimated by a factor of four (Figure 7A). The overestimation increases with enhanced wave strength, which is indicated by the H_s/h ratio, and 50% of the τ_{cw} values are overestimated by 1.6 times. When $H_s/h > 0.25$, the possibility of τ_{cw} being overestimated by 1.6 times is greater than 50%; when $H_s/h > 0.5$, the possibility increases to 90% (Figure 7B). This indicates that under low-energy wave conditions, when H_s/h is low, the assumption is still valid. The TKEw method offers the easiest approach to estimating τ_c by applying $w_t = w - w_m$. It also implies that it is reasonable for Kim et al. (2000) using the assumption as their measurement were carried out in the deeper site where H_s/h ratio is very small.

Figure 7

Studies of the wind effect on bed shear stress help to improve our understanding of sedimentary processes in intertidal areas. It has been widely observed and accepted that high winds increase wave heights significantly and result in an increase in wave orbital velocity, and thus τ_w (Gross et al., 1992; Janssen-Stelder, 2000; Dalyander et al., 2013). In a field study on a mudflat in the Dutch Wadden Sea, Janssen-Stelder (2000) found that high bed shear stress occurs around high water, when current velocity is low, and this enhanced bed shear stress is dominated by the wave-induced component. Our study shows that the mean τ_w contributed 40% to the mean τ_{cw} in windy conditions, while 15% in calm condition.

In shallow-water environments, breaking wave is an important cause of bed erosion. However, τ_w is estimated under non-breaking conditions. Field and laboratory studies have shown that when depth-limit wave-breaking occurs, wave-breaking generates turbulence and setup flow that can agitate substantial amounts of bed sediment, which leads to increase in suspended sediment concentration (Levoy et al., 2000; de Vries et al., 2008; Callaghan and Wainwright, 2013). However, it remains difficult to quantify the effect of breaking waves on bed erosion. In our case, the ratio of the height of largest 10% of waves to the water depth varies from 0.04 to 0.65; i.e., less than 0.73, and so indicates local non-breaking conditions (Battjes and Stive, 1985).

However, in addition to increasing the wave orbital motion, wind may affect the bed shear stress in another way because high values of τ_c were also found to occur around high water, when current velocities are low (Figure 6A). Using a regional-scale numerical modelling study of the Middle Atlantic Bight (USA), Dalyander et al. (2013) examined wind-driven currents by considering the correlation between non-tidal-induced stress and wind stress. This non-tidal term is usually caused by wind-driven flow. In our study, current speeds are still scaled with the water pressure gradient (Figure 2F and 2G). Therefore, in this case the wind-driven flow refers to turbulent flow rather than mean flow. The wind-driven turbulence cannot be captured by the LP method, which uses mean velocities, but it can be detected using the second momentum methods (TKE, TKEw, ID, and RS). These methods use the bulk turbulent velocities without separating the tidal-current-driven turbulence from the wind-driven turbulence. Therefore: (a) during slack water, the LP method results in low τ_c estimation, whereas the second momentum methods provide a τ_c of around 1 Pa (Figure 2I); and (b) under low-energy wave conditions, all methods are consistent, as the wind-driven motion is absent. This inference is supported by a recent wind-flume experiment, in which Su et al. (2015) pointed out that wind enhances the total bed shear stress by increasing the original vertical turbulence.

According to the acoustic principle, ADV measurements suffer from Doppler noise (Lohrmann et al., 1995). The Doppler noise level increases as the height closer to the bed because of the random scatter and velocity shear in the sampling volume (Voulgaris and Trowbridge, 1998). Moreover, the noise error with respect to vertical velocity variance is smaller than that for the horizontal velocity variance, by at least an order of magnitude (Kim et al., 2000). From this point of view, the TKEw method is less sensitive to errors caused by Doppler noise.

Finally, attention should be given to sampling duration and frequency, regardless of which second momentum method is selected. High- and low-frequency losses are caused by inappropriate sampling rates and sampling durations, respectively (Soulsby, 1980). A sampling duration of 90 s provides about 30 waves. The spectrum analysed here (Figures 3B and 4) is complete in the low-frequency domain. A low limit of 5 Hz was estimated for the sampling rate by Kim et al. (2000). In the present study, a sampling rate of 8 Hz was sufficient to avoid high-frequency losses.

By considering the intercomparison results and limitations mentioned above, we suggest a protocol to estimate the total bed shear stress, τ_{cw}, from ADV measurement data following Figure 8. Although the TKEw method associated with the ESA wave-turbulence decomposition technique is ideal for estimating τ_{cw}, we still suggest that several approaches should be applied to obtain the most reliable estimate of bed shear stress.

Figure 8

6. Conclusions

This paper presents a multi-approach method of estimating the total bed shear stress under combined wave and current action (τ_{cw}) based on in situ measurements of wave and current data. Using velocity spectrum analysis, we found that:

- The frequently used assumption that near-bed velocities in the vertical direction are not contaminated by waves is invalid during windy conditions. Our results demonstrate that when the ratio of significant wave height to water depth (H_s/h) is greater than 0.25, τ_{cw} is likely to be overestimated unless decomposition is used.
- During windy/stormy weather, winds enhance the total bed shear stress by: (1) levelling up τ_w by increasing the wave height; and (2) increasing τ_c by superimposing wind-driven turbulent velocities onto the original vertical velocities. This has significant effects on the models used to estimate total bed shear under combined wave–current action.
- ESA wave–turbulence decomposition method performs better than the MA method in terms of predicting turbulence energy spectrum which is used to obtain current-induced bed shear stress. On the other hand, the MA method can separate wave orbital velocities and turbulent velocities, so that it can provide the wave directions.
- The determination of the wave-induced bed shear stress (τ_w), which is dependent on probe type and deployment settings, is less arbitrary. In comparison, estimation

of the current-induced bed shear stress (τ_c) is dependent on the approach. All methods require measurements in the turbulent boundary layer. The LP method is the only approach that uses the mean components, but it is dependent on the velocity profile obeying a logarithmic law. Among the second momentum approaches, the ID method may give biased estimates because of the incomplete separation of shear production and energy dissipation, as well as the near-bed sediment concentration stratification. The TKE and ID methods are affected by Doppler noise in the horizontal direction, but we consider them to be the most consistent methods. The results of our intercomparison study, based on the index of agreement, indicate that the TKEw method, which incorporates the ESA decomposition technique, provides the best estimates of τ_{cw}.

We believe that the protocol proposed in the present study demonstrates that the ADV-approach has considerable potential to obtain reliable estimates of the total bed shear stress under combined wave–current action (τ_{cw}) in regions with complex hydrodynamics, such as intertidal flats. However, the probe height, sampling duration, and sampling frequency should be carefully chosen.

Acknowledgements

This study was funded by the Natural Science Foundation of China (No. 41576092, 41130856) and the Minstry of Science and Technology of China (2016YFA0600901). We thank Benwei Shi, Yingwen Liu, Chuangshou Wu, and Yajuan Li for assistance in the field, and Ruiming Wu for help with the grain size analysis. We also acknowledge NIOO-Yerseke for providing the Nortek 1.0-MHz ADCP. The authors also thank the anonymous reviewers for their suggestions and comments that helped improve this paper.

References

Andersen, T.J., Fredsoe, J., Pejrup, M., 2007. In situ estimation of erosion and deposition thresholds by Acoustic Doppler Velocimeter (ADV). Estuar. Coast. Shelf S. 75, 327-336.

Nortek AS, 2005. Vector Current Meter User Manual, Norway, p. 15.

Battjes, J.A., Stive, M.J.F., 1985. Calibration and verification of a dissipation model for random breaking waves. J. Geophys. Res. 90, 9159-9167.

Callaghan, D.P., Wainwright, D., 2013. The impact of various methods of wave transfers from deep water to nearshore when determining extreme beach erosion. Coast. Eng. 74, 50-58.

Christoffersen, J.B., Jonsson, I.G., 1985. Bed friction and dissipation in a combined current and wave motion. Ocean Eng. 12, 387-423.

Collins, M.B., Ke, X., Gao, S., 1998. Tidally-induced flow structure over intertidal flats. Estuar. Coast. Shelf S. 46, 233-250.

Dalyander, P.S., Butman, B., Sherwood, C.R., Signell, R.P., Wilkin, J.L., 2013. Characterizing wave- and current- induced bottom shear stress: U.S. middle Atlantic continental shelf. Continental Shelf Research 52, 73-86.

Davies, A.M., Gerritsen, H., 1994. An intercomparison of three-dimensional tidal hydrodynamic models of the Irish Sea. Tellus A 46, 200-221.

de Vries, J., van Gent, M.R.A., Walstra, D.J.R., Reniers, A., 2008. Analysis of dune erosion processes in large-scale flume experiments. Coast. Eng. 55, 1028-1040.

Fredsøe, J., 1984. Turbulent boundary layer in wave-current motion. J. Hydraul. Eng.-ASCE 110, 1103-1120.

Friedrichs, C.T., Wright, L.D., 1997. Sensitivity of bottom stress and bottom roughness estimates to density stratification, Eckernforde Bay, southern Baltic Sea. J. Geophys. Res.-Oceans 102, 5721-5732.

Friedrichs, C.T., Wright, L.D., 2004. Gravity-driven sediment transport on the continental shelfimplications for equilibrium profiles near river mouths. Coast. Eng. 51, 795-811.

Friedrichs, C.T., Wright, L.D., Hepworth, D.A., Kim, S.C., 2000. Bottom-boundary-layer processes associated with fine sediment accumulation in coastal seas and bays. Cont. Shlef Res. 20, 807-841.

Grant, W.D., Madsen, O.S., 1979. Combined wave and current interaction with a rough bottom. J. Geophys. Res.-Oceans and Atmospheres 84, 1797-1808.

Green, M.O., 1992. Spectral estimates of bed shear stress at subcritical Reynolds numbers in a tidal boundary layer. J. Phys. Oceanogr. 22, 903-917.

Green, M.O., Coco, G., 2007. Sediment transport on an estuarine intertidal flat: Measurements and conceptual model of waves, rainfall and exchanges with a tidal creek. Estuar. Coast. Shelf S. 72, 553-569.

Gross, T.F., Isley, A.E., Sherwood, C.R., 1992. Estimation of stress and bed roughness during storms on the Northern California Shelf. Cont. Shelf R. 12, 389-413.

Group of Shanghai Coastal Investigation (GCSI), 1988. Report of Shanghai Coastal Comprehensive Investigation. Shanghai Scientific and Technological Press, Shanghai (in Chinese).

Huntley, D.A., 1988. A modified inertial dissipation method for estimating seabed stresses at low Reynolds numbers, with application to wave/current boundary layer measurements. J. Phys. Oceanogr. 18, 339-346.

Huyng-Thanh, S., Temperville, A., 1990. A numerical model of the rough turbulent boundary layer in combined wave and current interaction. Coast. Eng. Proceedings 1.

Janssen-Stelder, B., 2000. The effect of different hydrodynamic conditions on the morphodynamics of a tidal mudflat in the Dutch Wadden Sea. Cont. Shelf R. 20, 1461-1478.

Kim, S.C., Friedrichs, C.T., Maa, J.P.Y., Wright, L.D., 2000. Estimating bottom stress in tidal boundary layer from Acoustic Doppler Velocimeter data. J. Hydraul. Eng.-ASCE 126, 399-406.

Lesser, G.R., Roelvink, J.A., van Kester, J., Stelling, G.S., 2004. Development and validation of a three-dimensional morphological model. Coast. Eng. 51, 883-915.

Levoy, F., Anthony, E.J., Monfort, O., Larsonneur, C., 2000. The morphodynamics of megatidal beaches in Normandy, France. Mar. Geol. 171, 39-59.

Liu, H., Wu, J.X., 2015. Estimation of bed shear stresses in the pearl river estuary. China Ocean Eng. 29, 133-142.

Lohrmann, A., Cabrera, R., Gelfenbaum, G., Haines, J., 1995. Direct measurements of Reynolds stress with an acoustic Doppler velocimeter. Proceedings of the IEEE Fifth Working Conference on Current Measurement (Cat. No.95CH35734), 205-210.

Meirelles, S., Henriquez, M., Hornerdevine, A.R., Souza, A.J., Pietrzak, J., Stive, M., 2015. Bed shear stress on the middle shoreface of the South-Holland coast. Coastal Sediments 2015. DOI: http://dx.doi.org/10.1142/9789814689977_0210

Myrhaug, D., Slaattelid, O.H., 1990. A rational approach to wave-current friction coefficients for rough, smooth and transitional turbulent flow. Coast. Eng. 14, 265-293.

O'Connor, B.A., Yoo, D., 1988. Mean bed friction of combined wave/current flow. Coast. Eng. 12, 1-21.

Salehi, M., Strom, K., 2012. Measurement of critical shear stress for mud mixtures in the San Jacinto estuary under different wave and current combinations. Cont. Shelf Res. 47, 78-92.

Sea-Bird Electronics, I., 2007. SBE 26plus Seagauge wave and tide recorder operating manual, Washington, USA, p. 5;92.

Shi, B., Wang, Y.P., Du, X., Cooper, J.R., Li, P., Li, M.L., Yang, Y., 2016. Field and theoretical investigation of sediment mass fluxes on an accretional coastal mudflat. J. Hydro-environ. Res. 11, 75-90.

Shi, B.W., Wang, Y.P., Yang, Y., Li, M.L., Li, P., Ni, W.F., Gao, J.H., 2015. Determination of Critical Shear Stresses for Erosion and Deposition Based on In Situ Measurements of Currents and Waves over an Intertidal Mudflat. J. Coast. R. 31, 1344-1356.

Soulsby, R., 1997. Dynamics of marine sands: a manual for practical applications. Thomas Telford.

Soulsby, R., Humphery, J., 1990. Field observations of wave-current interaction at the sea bed, Water wave kinematics. Springer, pp. 413-428.

Soulsby, R.L., 1980. Selecting record length and digitization rate for near-bed turbulence measurements. J. Phys. Oceanogr. 10, 208-219.

Soulsby, R.L., 2005. Bed shear-stresses under combined waves and currents on smooth and rough beds., HR Wallingford, Hydraulics research report TR 137.

Stapleton, K., Huntley, D., 1995. Seabed stress determinations using the inertial dissipation method and the turbulent kinetic energy method. Earth Surf. Proc. Land. 20, 807-815.

Su, M., Yao, P., Wang, Z.B., Chen, Y.P., Zhang, C.K., Stive, M.J.F., 2015. Laboratory studies on the response of fine sediment to wind, IAHR World Congress 2015. IHAR, the Netherlands.

van Rijn, L.C., 1993. Principles of sediment transport in rivers, estuaries and coastal seas. Aqua Publication, Amsterdam, the Netherlands.

Verney, R., Brun-Cottan, J.C., Lafite, R., Deloffre, J., Taylor, J.A., 2006. Tidally-induced shear stress variability above intertidal mudflats in the macrotidal Seine estuary. Estuar. Coast. 29, 653-664.

Villaret, C., Latteux, B., 1992. Long-term simulation of cohesive sediment bed erosion and deposition by tidal currents. Long-term simulation of cohesive sediment bed erosion and deposition by tidal currents, 19 pp.

Voulgaris, G., Trowbridge, J.H., 1998. Evaluation of the acoustic Doppler velocimeter (ADV) for turbulence measurements. J. Atmos. Ocean. Technol. 15, 272-289.

Wang, Y.P., Gao, S., Jia, J., Thompson, C.E.L., Gao, J., Yang, Y., 2012. Sediment transport over an accretional intertidal flat with influences of reclamation, Jiangsu coast, China. Mar. Geol. 291, 147-161.

Wang, Y.P., Gao, S., Jia, J.J., 2006. High-resolution data collection for analysis of sediment dynamic processes associated with combined current-wave action over intertidal flats. Chinese Sci. Bull. 51, 866-877.

Wang, Y.P., Voulgaris, G., Li, Y., Yang, Y., Gao, J.H., Chen, J., Gao, S., 2013. Sediment resuspension, flocculation, and settling in a macrotidal estuary. J. Geophys. Res.-Oceans 118, 5591-5608.

Wang, Y.Y., 2007. The Observations and Models of Bottom Boundary Layer for Fine Sediment, State Key Laboratory of Estuarine and Coastal Research. East China Normal University, Shanghai, China, p. 126. (in Chinese)

Warner, J.C., Sherwood, C.R., Signell, R.P., Harris, C.K., Arango, H.G., 2008. Development of a three-dimensional, regional, coupled wave, current, and sediment-transport model. Comput. Geosci. 34, 1284-1306.

Whitehouse, R., Soulsby, R., Roberts, W., Mitchener, H., 2000. Dynamics of estuarine muds: A manual for practical applications. Tomas Telford Limited, 1 Heron Quay, London.

Wilkinson, R., 1985. Variation of roughness length of a mobile sand bed in a tidal flow. Geo-mar. Lett. 5, 231-239.

Williams, J.J., Bell, P.S., Thorne, P.D., 2003. Field measurements of flow fields and sediment transport above mobile bed forms. J. Geophys. Res.-Oceans 108, 36.

Willmott, C.J., 1981. On the validation of models. Phys. Geogr. 2, 184-194.

Yang, S.L., Li, H., Ysebaert, T., Bouma, T.J., Zhang, W.X., Wang, Y., Li, P., Li, M., Ding, P., 2008. Spatial and temporal variations in sediment grain size in tidal wetlands, Yangtze Delta: On the role of physical and biotic controls. Estuar. Coast. Shelf Sci. 77, 657-671.

Yang, S.L., Milliman, J.D., Li, P., Xu, K., 2011. 50,000 dams later: Erosion of the Yangtze River and its delta. Global Planet. Change 75, 14-20.

Zhu, Q., Yang, S., Ma, Y., 2014. Intra-tidal sedimentary processes associated with combined wave–current action on an exposed, erosional mudflat, southeastern Yangtze River Delta, China. Mar. Geol. 347, 95-106.

Table 1. Statistics and inter-comparison (index of agreement, I) of wave-induced bed shear stress, τ_w.

		SBE	ADV: 0-crossing	ADV: spectral
τ_{cw} (Pa)	Mean	0.28	0.25	0.22
	Std.	0.16	0.22	0.18
I	SBE	1	0.94	0.94
	ADV: 0-crossing	0.94	1	0.98
	ADV: spectral	0.94	0.98	1

Table 2. Inter-comparison (index of agreement, *I*) of τ_c in calm and windy conditions, and τ_{cw} in the whole measurement duration. In the WCI model, τ_w was obtained from spectral estimation using ADV measured pressure data. The following methods were used to estimate τ_c: TKE: turbulent kinetic energy; TKEw: modified TKE using vertical turbulent velocity only; ID: Inertial dissipation; and RS: Reynolds shear stress. The wave–turbulence decomposition methods used were moving averages (MA) and energy spectrum analysis (ESA).

	Method		LP	TKE		TKEw		ID	RS	Mean
				MA	ESA	MA	ESA	MA		
$I-\tau_c$ Calm	LP		1	0.50	0.85	0.86	0.97	0.88	0.89	0.85
	TKE	MA	0.57	1	0.82	0.83	0.64	0.78	0.62	0.75
		ESA	0.85	0.82	1	0.95	0.80	0.94	0.90	0.89
	TKEw	MA	0.86	0.82	0.95	1	0.89	0.98	0.81	0.90
		ESA	0.97	0.58	0.80	0.89	1	0.88	0.73	0.84
	ID	MA	0.88	0.77	0.94	0.98	0.88	1	0.81	0.89
	RS		0.89	0.61	0.90	0.81	0.74	0.80	1	0.82
$I-\tau_c$ Windy	LP		1	0.51	0.36	0.54	0.54	0.33	0.61	0.56
	TKE	MA	0.51	1	0.67	0.71	0.58	0.66	0.38	0.64
		ESA	0.38	0.68	1	0.81	0.82	0.72	0.36	0.68
	TKEw	MA	0.55	0.72	0.81	1	0.86	0.79	0.39	0.73
		ESA	0.56	0.58	0.82	0.86	1	0.77	0.49	0.73
	ID	MA	0.36	0.65	0.72	0.79	0.77	1	0.37	0.67
	RS		0.62	0.35	0.34	0.37	0.46	0.35	1	0.50
$I-\tau_{cw}$ All	LP		1	0.72	0.64	0.73	0.75	0.58	0.76	0.74
	TKE	MA	0.72	1	0.85	0.87	0.71	0.83	0.70	0.81
		ESA	0.65	0.86	1	0.91	0.87	0.85	0.65	0.83
	TKEw	MA	0.74	0.87	0.91	1	0.90	0.89	0.65	0.85
		ESA	0.76	0.73	0.87	0.90	1	0.84	0.63	0.82
	ID	MA	0.60	0.83	0.85	0.89	0.83	1	0.60	0.80
	RS		0.76	0.70	0.64	0.64	0.62	0.59	1	0.71
τ_{cw} (Pa)	Mean		0.63	0.90	0.68	0.69	0.65	0.72	0.79	0.74[a]
	Std.		0.50	0.56	0.41	0.41	0.39	0.49	0.59	0.48[a]

a. Results from the LP method are excluded as the related instrument ADCP covered less time measurement periods than ADV.

Appendix A: Tables

Table A.1. Approaches employed to obtain the wave parameters used in Equations (3)–(5).

		ADV	
	SBE-26plus	**Zero-crossing method** (Tucker and Pitt, 2001)	**Spectral method** (Wiberg and Sherwood, 2008)
Wave height, H	SEASOFT for Waves (Sea-Bird Electronics Inc.)	H_s: mean wave height of highest 33%	$H_s = 4\sqrt{\sum_i S_h(f_i)\Delta f_i}$
Wave period, T		T_s: mean wave period of highest 33%	$1/T_{br} = f_{br} = \frac{\sum_i \left[f_i \frac{4\pi^2}{T_i^2 \sinh^2(k_i h)} S_{h,i}\Delta f_i \right]}{\sum_i \left[\frac{4\pi^2}{T_i^2 \sinh^2(k_i h)} S_{h,i}\Delta f_i \right]}$
Bottom orbital velocity, U_δ	U_δ: Equation (4)		$U_\delta = 2\sqrt{\sum_i \left[\frac{4\pi^2}{T_i^2 \sinh^2(k_i h)} S_{h,i}\Delta f_i \right]}$

Table A.2. Second momentum methods used to estimate the current-induced bed shear stress, τ_c

Method	Formula	Parameters and coefficients
TKE Turbulent kinetic energy	$TKE = \frac{1}{2}\rho_w(\overline{u_t^2} + \overline{v_t^2} + \overline{w_t^2})$ $\tau_{c,TKE} = C_1 \cdot TKE$	C_1=0.19 (Stapleton and Huntley, 1995)
TKEw Vertical turbulent kinetic energy	$\tau_{c,TKEw} = C_2\rho_w\overline{w_t^2}$	C_2=0.9 (Kim et al., 2000)
RS Reynolds stress	$\tau_{c,RS} = \rho_w\sqrt{\overline{u_f w_f}^2 + \overline{v_f w_f})^2}$	u_f v_f w_f : total fluctuating velocities, i.e., $u_f = u_w + u_t$
ID Inertial dissipation	$U_* = (\frac{2\pi\kappa z}{U_c})^{1/3}\left(\frac{S_{w'}(f)f^{5/3}}{\alpha_3}\right)^{1/2}$ $\tau_{c,ID} = \rho_w U_*^2$	κ=0.4 $\alpha_3 = 0.68$ (Green, 1992)

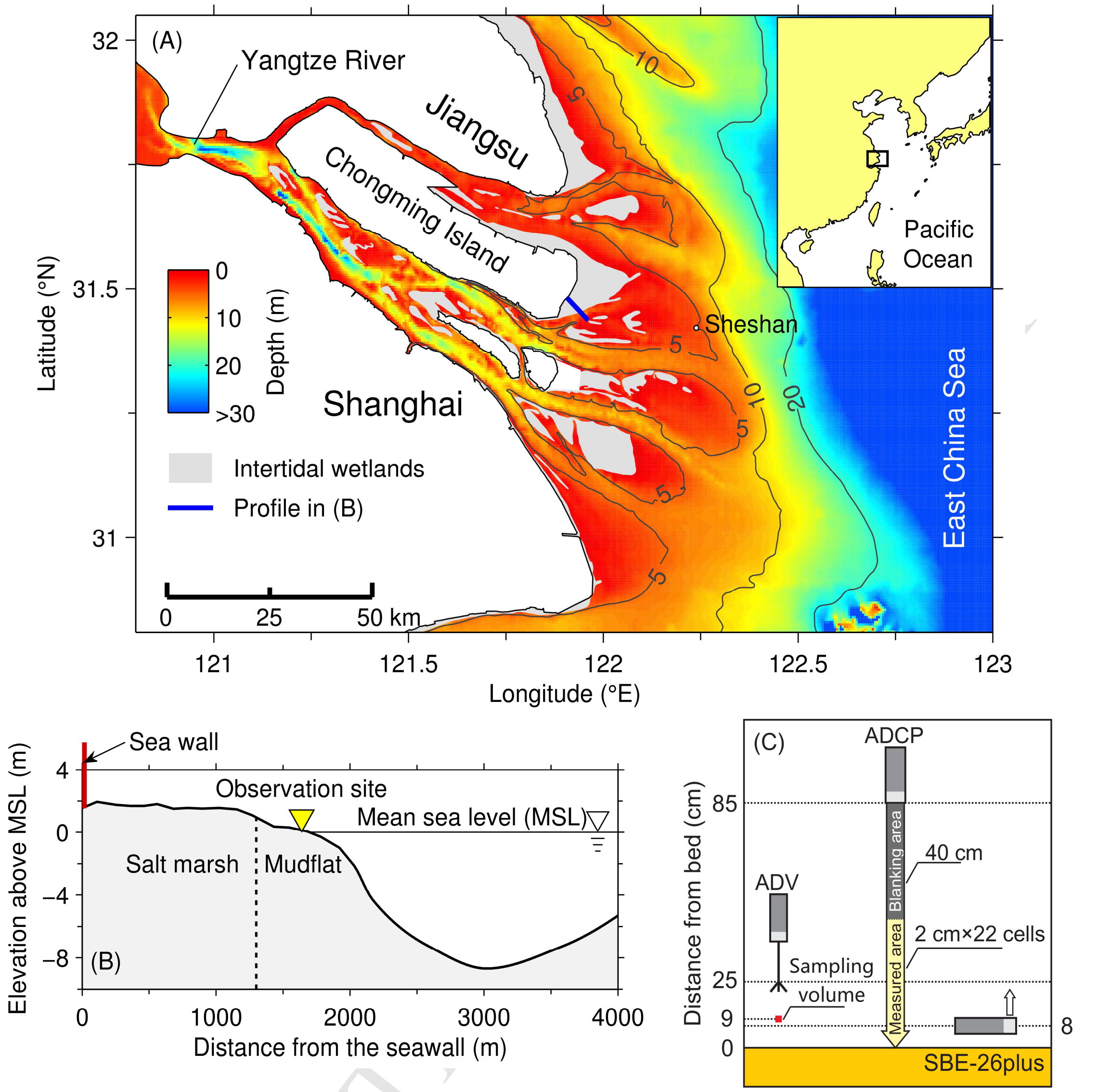

Figure 1. (A) Map of the Yangtze River Delta showing the observation site. (B) Cross-shore bathymetric profile of the observation site. The elevation datum is the lowest astronomic tide (LAT). (C) Schematic representation of instrument deployment and location with respect to the seabed. The SBE-26plus was used to obtain water depth and wave parameters, the ADCP to measure velocity profiles, and the ADV for the high-frequency sampling of both pressure and velocity data at 8 Hz. Lighter parts of the rectangles, which represent the locations of the instruments, indicate the locations of sensors. Arrows indicate the direction each sensor faced.

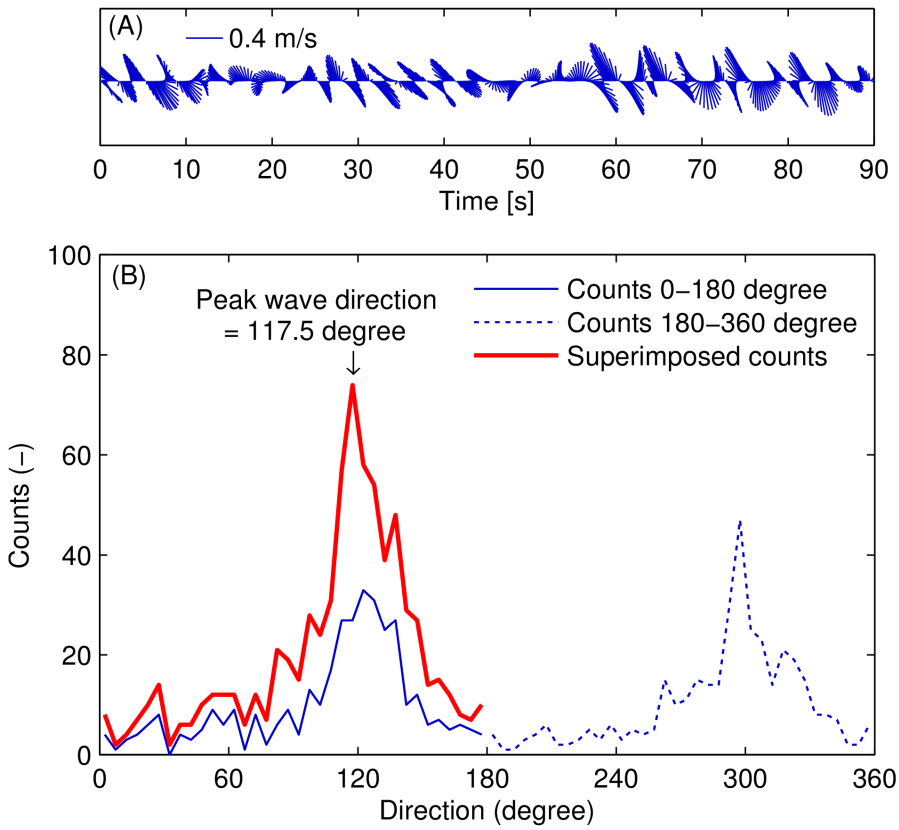

Figure 2. (A) Vector series of near-bottom wave orbital velocity filtered from the ADV in a burst, and (B) its direction (in Cartesian coordinates) count.

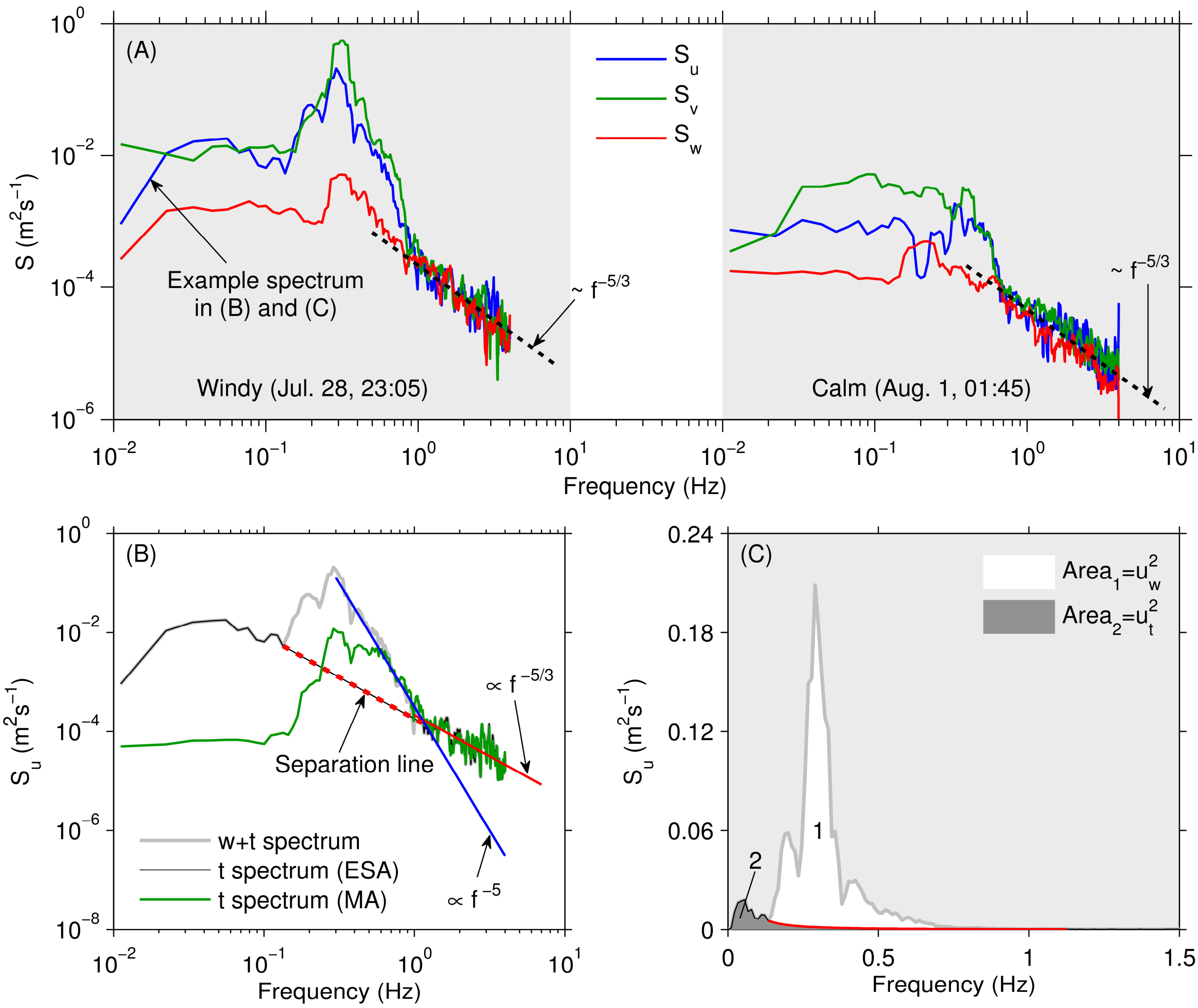

Figure 3. (A) Examples of energy spectra of combined wave orbital and turbulent velocities of three directions in windy and calm conditions, respectively. (B) An example of ESA and MA methods decomposed turbulent velocity spectra. The energy spectrum of combined wave orbital and turbulent velocities comprises a conventional turbulence spectrum (with a $f^{-5/3}$ power law behaviour in the inertial subrange) and a wave velocity spectrum (with a f^{-5} power law behaviour at higher wave bands). (C) The same spectra as in (B) plotted on linear axes. The wave variance $\overline{u_w^2}$ is given by the area between the dividing line, the red dotted line in (B), and the spectrum, with the remaining area being the turbulent variance $\overline{u_t^2}$.

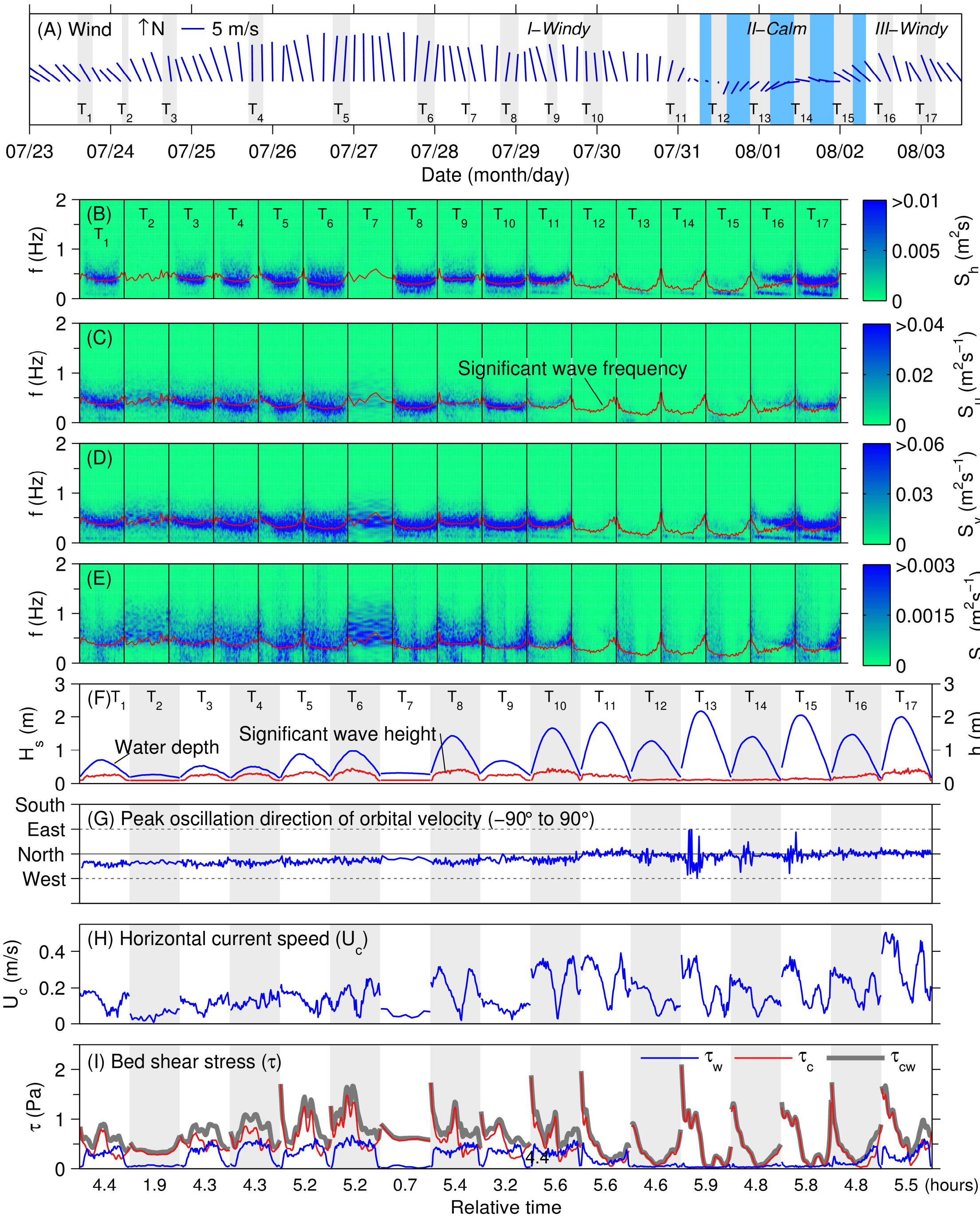

Figure 4. Time series of (A) wind vectors, (B) the energy spectrum of water depth, and (C–E) energy spectra of combined wave orbital and turbulent velocities in the east, north, and vertical up directions, (F) water depth (h) and significant wave height (H_s), (G) horizontal current speed (U_c), (H) wave oscillation directions, and (I) wave/current-induced bed shear stresses (τ_w and τ_c, respectively) and total bed shear stress (τ_{cw}). Each time series section covers the period of a single tidal inundation.

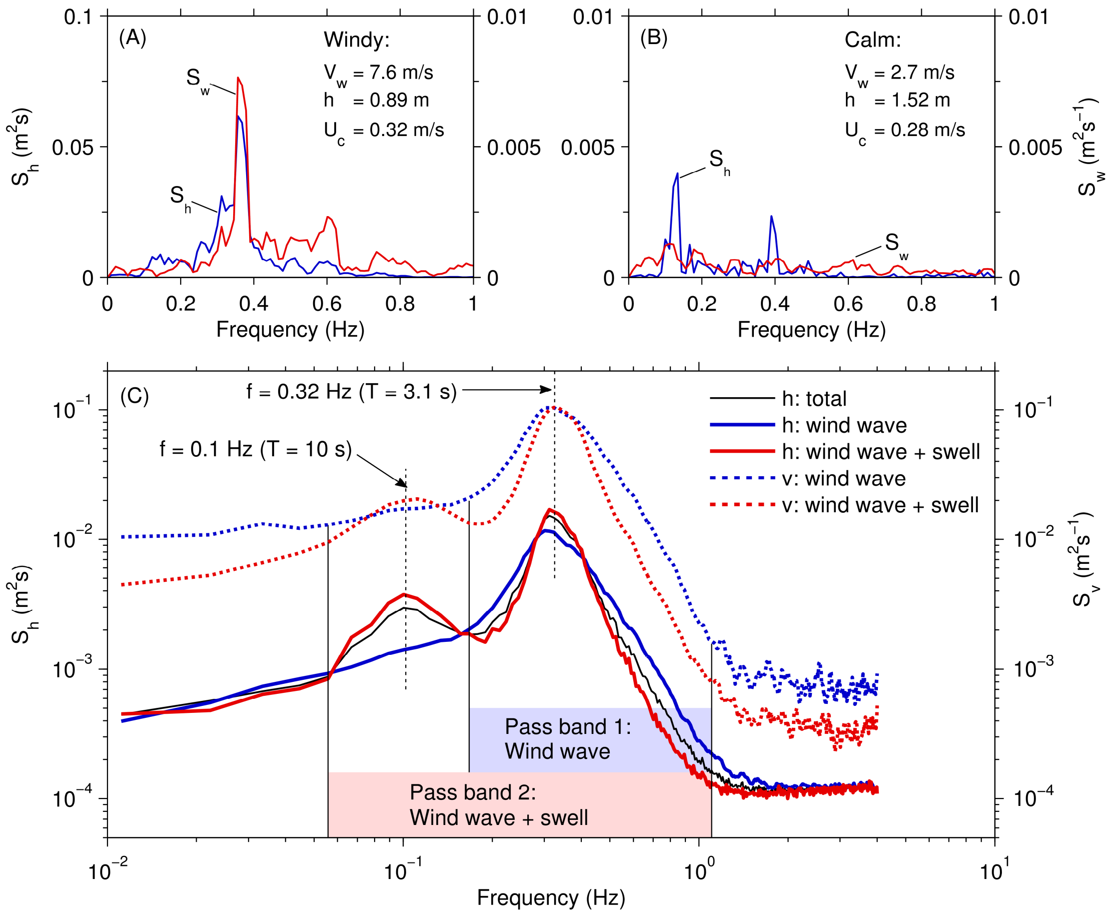

Figure 5. (A) and (B) show water depth and vertical velocity spectra in typical bursts of windy conditions and calm conditions, respectively. V_w, h, and U_c are wind speed, water depth, and horizontal current speed, respectively. (C) shows mean wave spectra showing that local waves are driven by wind during windy weathers (before July 31), but by both wind and swells during calm weathers (after July 31). Two corresponding pass-bands were used to carry out velocity spectra filtration.

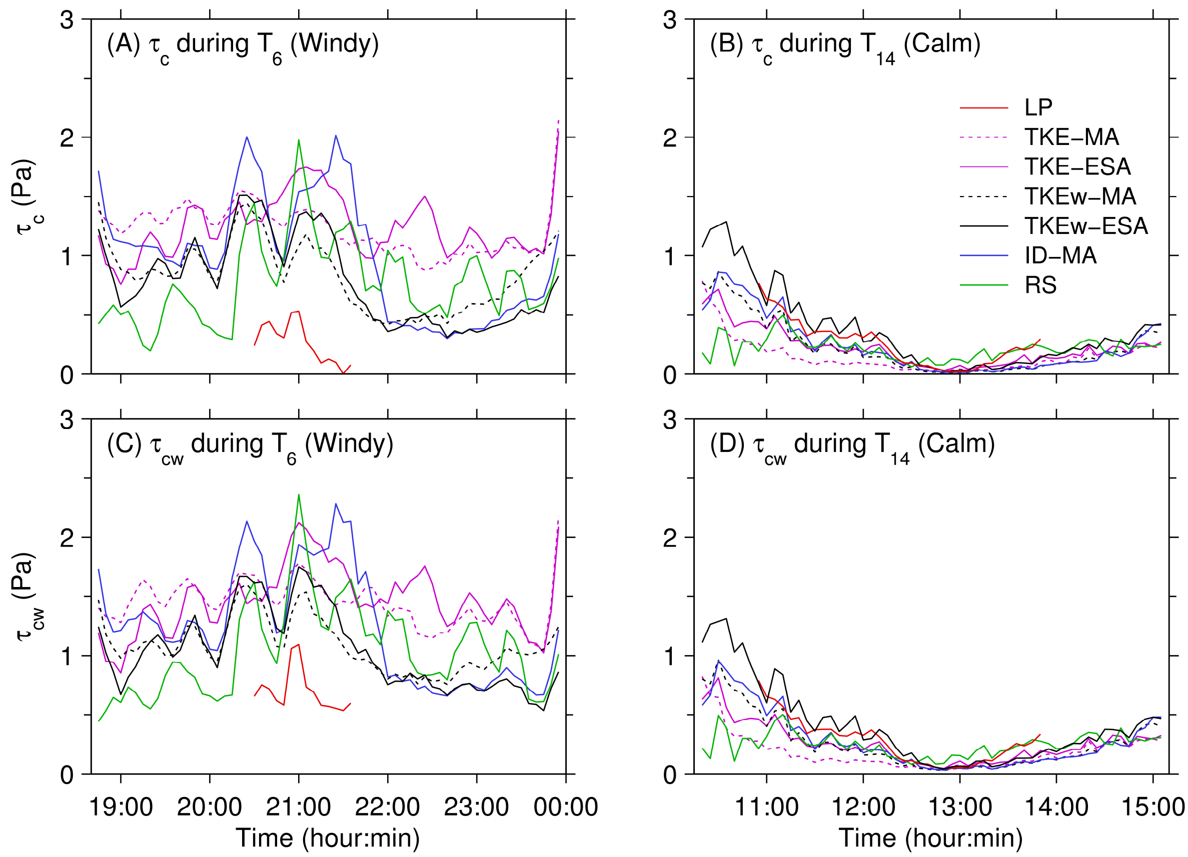

Figure 6. Expanded sections of the time series of τ_c and τ_{cw} obtained using the various approaches. The two tidal cycles are representative because tidal-average τ_{cw} in the cycle in July 28th and August 1st reaches maximum in windy period and minimum in calm period, respectively. Legends in panels (A), (C) and (D) are the same as that in panel (B).

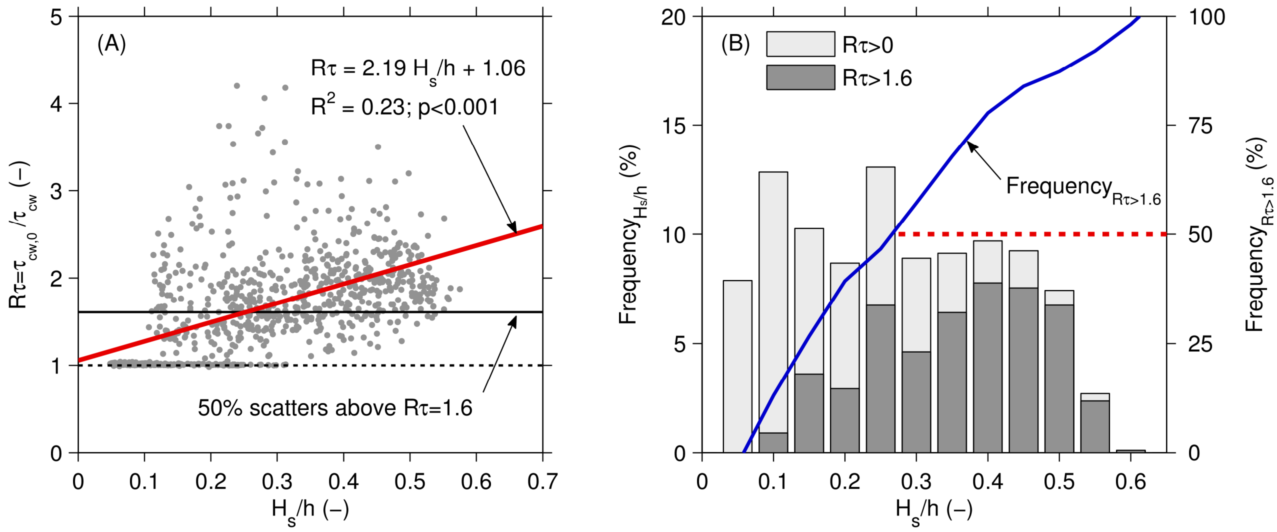

Figure 7. (A) The ratio of total bed shear stress without and with wave-turbulence decomposition (Rτ = $\tau_{cw,0}/\tau_{cw}$) increases with the ratio of significant wave height to water depth (H_s/h). Fifty percent of the τ_{cw} values are overestimated by 1.6 times. (B) Frequency diagram of H_s/h shows that Rτ > 1.6 probably occurs in the higher H_s/h domain. When H_s/h > 0.25, the possibility of the τ_{cw} value being overestimated by 1.6 times is greater than 50%.

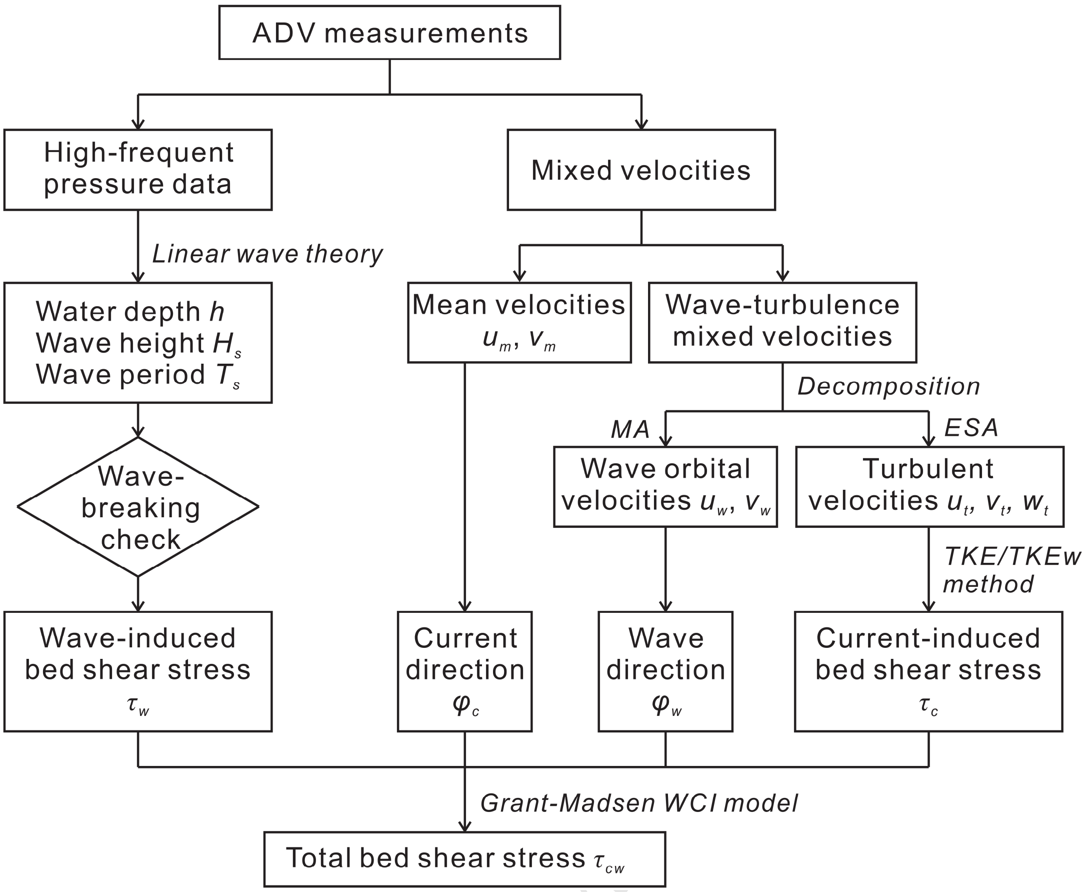

Figure 8. Protocols for estimating total bed shear stress under combined wave–current action, τ_{cw}, using in situ ADV data.

Highlights

1. The most widely used theories are tested to obtain total bed shear stresses.
2. Wind enhances both the wave and current induced bed shear stresses.
3. Near-bed vertical velocity fluctuations are contaminated by surface waves.
4. A solution is proposed to obtain current bed shear stress from in situ ADV data.